nature communications

Article

https://doi.org/10.1038/s41467-024-52205-9

Hybrid lipid-AuNP clusters as highly efficient SERS substrates for biomedical applications

Received: 20 October 2023

Accepted: 29 August 2024

Published online: 12 September 2024

Check for updates

Jacopo Cardellini[1,7,9], Caterina Dallari[2,3,4,9], Ilaria De Santis[1], Lorenzo Riccio[1,8], Costanza Ceni[1,2], Amelia Morrone[5,6], Martino Calamai[2,4], Francesco Saverio Pavone[2,3,4], Caterina Credi[2,4], Costanza Montis[1] & Debora Berti[1]

Although Surface Enhanced Raman Scattering (SERS) is widely applied for ultrasensitive diagnostics and imaging, its potential is largely limited by the difficult preparation of SERS tags, typically metallic nanoparticles (NPs) functionalized with Raman-active molecules (RRs), whose production often involves complex synthetic approaches, low colloidal stability and poor reproducibility. Here, we introduce LipoGold Tags, a simple platform where gold NPs (AuNPs) clusters form via self-assembly on lipid vesicle. RRs embedded in the lipid bilayer experience enhanced electromagnetic field, significantly increasing their Raman signals. We modulate RRs and lipid vesicle concentrations to achieve optimal SERS enhancement and we provide robust structural characterization. We further demonstrate the versatility of LipoGold Tags by functionalizing them with biomolecular probes, including antibodies. As proof of concept, we successfully detect intracellular GM1 alterations, distinguishing healthy donors from patients with infantile GM1 gangliosidosis, showcasing LipoGold Tags as advancement in SERS probes production.

In recent decades, surface enhanced Raman spectroscopy (SERS) has emerged as a versatile and robust analytical tool, finding applications spanning environmental science, biology, and nanomedicine[1,2]. The unique advantages of SERS, including its exceptional sensitivity, specificity and access to biochemical information, have positioned SERS-based techniques as powerful optical diagnostic tool, enabling a valuable alternative to conventional diagnostic methods like fluorescence-based spectroscopy[3,4]. It is well known that Raman signals of molecules adsorbed on nanostructured metallic surfaces can undergo signal enhancement by several orders of magnitude (from 10^2 to 10^{10}, depending on substrate type) due to the amplification of the electromagnetic field resulting from the Localized Surface Plasmon Resonance effect[5,6]. Among various metallic nanoparticles (NPs), gold nanoparticles (AuNPs) emerge as the most efficient substrates for ultrasensitive SERS detection[7], while only few example of non-plasmonic structures have been proposed as they generally present weaker and less efficient field enhancement, limited tunability, and stability issues[8]. Metallic NPs can be functionalized with Raman-active dye molecules (Raman Reporters, RRs), characterized by narrow Raman peaks, thereby forming "SERS tags", which serve as contrast agents in bioimaging applications[9–17], and function as sensing probes targeting minute analyte concentrations in diluted liquid samples[18–23]. Furthermore, the aggregation of NPs into fractal architectures introduces additional enhancement, creating localized hotspots at NPs'

[1]Department of Chemistry "Ugo Schiff" and CSGI, University of Florence, Florence, Italy. [2]European Laboratory for Non-Linear Spectroscopy (LENS), Sesto Fiorentino, Italy. [3]Department of Physics, University of Florence, Sesto Fiorentino, Italy. [4]National Institute of Optics—National Research Council, Sesto Fiorentino, Italy. [5]Laboratory of Molecular Biology of Neurometabolic Diseases, Neuroscience Department, Meyer Children's Hospital IRCCS, Florence, Italy. [6]Department of Neurosciences, Psychology, Drug Research and Child Health (NEUROFARBA), University of Florence, Florence, Italy. [7]Present address: Department of Chemistry and Applied Biosciences, Institute for Chemical and Bioengineering, ETH Zurich, Zurich, Switzerland. [8]Present address: Institute of Organic Chemistry, Faculty of Chemistry, University of Vienna, Vienna, Austria. [9]These authors contributed equally: Jacopo Cardellini, Caterina Dallari. e-mail: debora.berti@unifi.it

junctions[24–26]. Despite the great potential, the fabrication of SERS tags, particularly those containing NPs clusters, is still extremely challenging[27–30]. These tags must retain colloidal stability, biocompatibility, and specificity, even after surface functionalization with RRs. RRs, often organic hydrophobic molecules, can compete with NP-stabilizing ligands, compromising colloidal stability[31,32]. Consequently, Raman tags based on NPs' clusters necessitate a delicate balance of the RRs/stabilizer ratio to ensure a robust SERS signal without inducing uncontrolled aggregation[25]. Numerous smart and effective strategies have been proposed for fabricating efficient SERS tags with high targeting efficiency and SERS intensity, as well as long-term colloidal stability[33–38]. However, these methods often involve time-consuming and multiple-step syntheses that may lead to NP aggregates lacking in reproducibility and structural stability, usually dependent on the RR chemical structure[32]. In the present work, we propose a simple, reproducible, and versatile strategy for developing controlled RRs-AuNPs clusters as SERS probes simultaneously ensuring high SERS performances and structural and colloidal stability.

In terms of NPs' controlled aggregation, there are some recent reports on the spontaneous formation of AuNP clusters on the lipid membrane of natural and synthetic vesicles[39–43]. The vesicle bilayer induces the formation of AuNPs-vesicle adducts, offering precise control over AuNPs-vesicle aggregate formation, compactness, and colloidal stability through modulation of vesicle composition and concentration[44–46]. The formation of such AuNPs-vesicle hybrids combines the biocompatibility and encapsulation capabilities of lipid scaffolds, extensively employed for embedding hydrophobic and hydrophilic drugs, with the diverse properties of inorganic NPs, such as electric, optical, magnetic, and catalytic functionalities. Furthermore, this synthesis method readily includes the introduction of targeting functionalities by conjugating antibodies to the liposomal surface through covalent and non-covalent interactions, resulting in multifunctional nanomaterials with potential simultaneous applications in diagnostics, imaging, and immunotherapy[47,48].

Here, based on our knowledge on the spontaneous clustering of citrate-coated gold nanoparticles on lipid vesicles, we designed a hybrid system (LipoGold tags) where the interplay between different interfacial forces enables building-up an efficient, versatile, and multifunctional SERS probe via simple self-assembly steps, that overcome all the drawbacks mentioned. Specifically, three distinct interfacial phenomena lead to the spontaneous formation of the final construct:

(i) with a similar strategy as the common inclusion of hydrophobic drugs in liposomal vectors, the hydrophobic Raman reporter molecules are included in the lipid membrane, due to hydrophobic interactions. This allows avoiding exposure of RRs towards the water solution, improving solubility, and avoiding significant sample-to-sample differences especially when changing RR structure.

(ii) liposomes loaded with the Raman reporter are exposed to citrate-coated AuNPs, leading to the controlled clustering of AuNPs on the liposomal surface and the formation of SERS hotspots.

(iii) finally, the Raman reporter, which is freely diffusing inside the liposomal membrane, is able to encounter the AuNPs clusters and attach to them via its thiol moiety, ensuring the close proximity between the Raman reporter and the SERS hotspots, which is necessary for efficient SERS enhancement.

The lipid bilayer is used as a scaffold to encapsulate RRs and induce AuNP spontaneous clustering, enabling RRs exposure to the enhanced electromagnetic field. The inclusion of hydrophobic RRs within the bilayer is straightforward and circumvents phase transfer steps minimizing the competition with ligands on the Au surface. The synergistic combination of these individual components offers unique advantages for SERS-based imaging and detection.

First, we varied both RRs and lipid vesicles' concentrations to optimize the SERS enhancement by comparing the plasmonic properties and the Raman signal of the adducts. Then, the LipoGold tags were characterized in terms of morphology, colloidal stability, and reproducibility of the synthetic protocol through techniques such as Cryogenic Electron Microscopy (Cryo-EM) and Dynamic Light Scattering (DLS). Moreover, the versatility of the approach is demonstrated across diverse hydrophobic RRs, highlighting its broad applicability. Further expanding the approach, the LipoGold tags tunability is then harnessed to functionalize them with probes directed at specific cellular components, introducing targeting capabilities. Validated through Fluorescence Correlation Spectroscopy (FCS) and a tailored sandwich assay, this approach's efficacy is confirmed in an in vitro setting, where the SERS signal and specificity are retained within cell cultures. Finally, we demonstrate the ability of LipoGold tags to detect GM1 alterations in fibroblast from healthy donors and patient affected by infantile GM1 gangliosidosis, a rare metabolic pathology manifesting GM1 intracellular accumulation, by easily modifying the LipoGold tag surface with the Cholera Toxin Subunit B-FITC™ (CT-B), a fluorescently labeled protein that specifically binds the GM1 ganglioside. Overall, this work presents a highly straightforward strategy, based on simple and rapid self-assembly for creating AuNPs-vesicle hybrid materials for SERS applications, addressing current challenges in the fabrication of metallic nanoarrays.

Results and discussion

Preparation of LipoGold tags

A conceptual scheme of the LipoGold tag design is illustrated in Fig. 1a. We explored several liposomal formulations to host the RR. Specifically, four liposomes' types were tested, composed of DOPC or POPC, which assemble into soft liquid-crystalline bilayers, and DSPC or DPPC, known to form rigid gel phase membranes in water. The lipid vesicles were prepared with a standardized methodology, involving the dissolution of the lipids in an organic solvent ($CHCl_3$/MeOH mixture, refer to Methods for detailed procedures), which is then evaporated to yield a lipid film; the film is then rehydrated followed by extrusion, to minimize lamellarity and polydispersity. RRs are small molecules, generally characterized by a pronounced hydrophobicity, deriving from the presence of aromatic groups, responsible for the Raman-active signals. A common RR employed to build-up SERS probes is 4-Mercaptobenzoic acid (4-MBA). To effectively integrate a hydrophobic RR within a liposomal membrane, a simple method involves co-dissolution, leading to a dry lipid film containing the RR. Upon hydration, the RR remains confined within the liposomal membrane[49]. Employing this technique, DOPC, POPC, DPPC, and DSPC liposomes embedding 4-MBA in the bilayer were prepared. To assess the capability of RR-laden liposomes to induce AuNPs' clustering, AuNPs dispersion were mixed with DOPC, POPC, DPPC, and DSPC liposomes containing 1% 4-MBA mol/mol (see supplementary Figs. 1-2 for AuNPs characterization). This interaction resulted in an abrupt shift in the characteristic color of AuNPs, from red to purple/blue, depending on the lipid composition. Figure 1b presents UV-visible spectra of AuNPs collected after 30 min interaction with DOPC, POPC, DPPC, and DSPC liposomes. Clearly, the spectral features varied significantly, depending on the rigidity of the vesicles' bilayer. Specifically, the interaction of AuNPs with rigid vesicles (DPPC and DSPC) induced minimal plasmonic alterations, ascribable to changes in the AuNPs' dielectric environment following adhesion to the lipid membrane. Conversely, AuNPs incubated with soft vesicles (DOPC and POPC), exhibit more pronounced plasmonic variations. The dispersion color immediately turned blue, and the spectra displayed the appearance of a shoulder (POPC, red curve) or even a well-defined, red-shifted peak (DOPC, black curve). These spectral modifications are consistent with the formation of AuNPs' clusters, whose occurrence is templated by the lipid membrane[44,46,50,51]. To visualize the AuNPs-liposome hybrids, Cryo-EM measurements were performed and representative Cryo-EM micrographs of AuNPs-DOPC and AuNPs-DPPC hybrids are presented in Fig. 1c, d, respectively. Across all cases, AuNPs adhere directly to the

https://doi.org/10.1038/s41467-024-52205-9

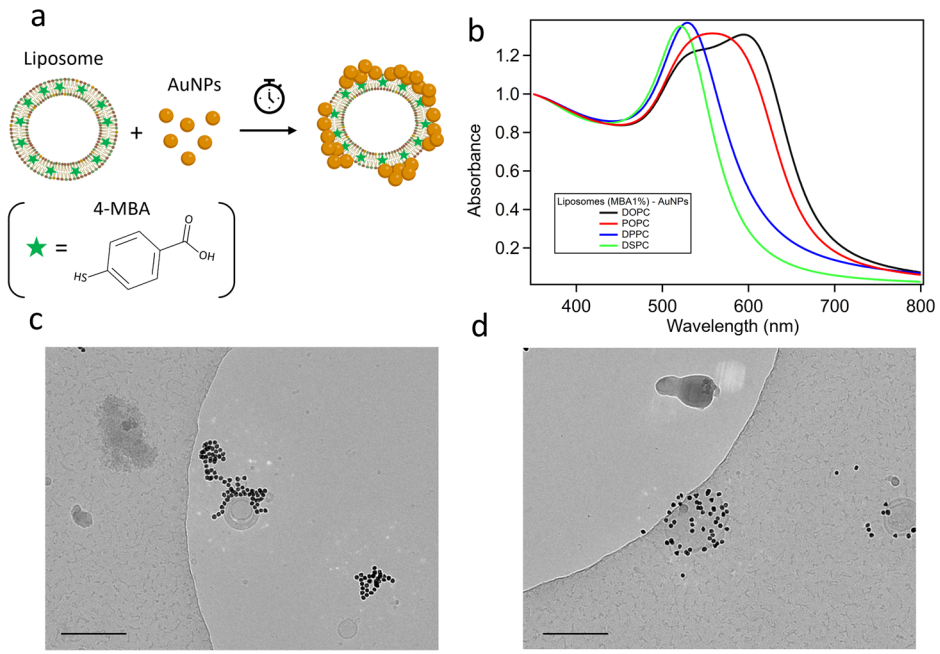

Fig. 1 | Self-assembly of AuNPs on liposomes with different membrane rigidity. **a** Graphical representation of the proposed approach to form LipoGold SERS tags; (**b**) UV-visible spectra of 6 nM AuNPs containing 1.2 nM (DOPC(MBA) black, POPC(MBA) red, DPPC(MBA) blue, and DSPC(MBA) green) liposomes collected after 30 min of incubation; Cryo-EM images showing (**c**) AuNPs-DOPC and (**d**) AuNPs-DPPC adducts. Scale bar is 200 nm. Cryo-TEM representative experiments have been repeated 2 times. See SI for additional images. Source data are provided as a Source Data file.

lipid bilayer without causing membrane disruption. In line with the plasmonic variations, AuNPs' interaction with soft DOPC(MBA) membranes leads to the formation of compact clusters where AuNPs are in direct contact. In contrast, interaction with rigid liposomes resulted in AuNPs adhering onto DPPC(MBA) membranes as individual entities, exhibiting larger interparticle spacing. Since these experimental results align with our recent studies on liposome-AuNPs interaction in the absence of RRs[44,46], it is reasonable to infer that the presence of MBA molecules embedded in the lipid bilayer does not substantially affect the overall interaction mechanism between citrate-capped AuNPs and zwitterionic vesicles.

SERS signals were collected through Confocal Raman microscopy from the dispersions. Figure 2a displays the MBA Raman signals (localized at 1069 cm^{-1} and 1577 cm^{-1}). While the RRs' intensity would negligibly vary under these experimental conditions, independently of the liposomal formulation where the probe is included (Supplementary Fig. 5), for LipoGold tags the Raman signal underwent dramatic enhancement. This enhancement can be attributed to a close interaction between MBA and AuNPs, driven by the MBA thiol pendant group. To corroborate such hypothesis, we monitored plasmonic and Raman variations of AuNPs interacting with liposomes containing Benzoic Acid (BA). As shown in Supplementary Fig. 10, while the plasmonic features of the DOPC-AuNPs are not dramatically affected by the presence of BA or MBA molecules, the Raman signal for BA-containing liposomes disappears. Consequently, it is reasonable to assume that the RR experiences the intense electric field generated by the plasmon resonance near the Au surface, leading to an amplified Raman signal due to the SERS effect (Fig. 2a). Remarkably, the Raman spectra collected for each sample, despite their nearly identical phospholipid compositions, displayed significant differences. This evidence is clear in Fig. 2b, where the Raman intensity of the MBA closely mirrors the aggregation trend of AuNPs displayed in Fig. 1b. Specifically, as NPs aggregation on the lipid surface increased with decreasing vesicles' stiffness (from DSPC to DOPC), the Raman intensity of both MBA peaks intensified. This occurrence can be attributed to the emergence of new hot spots within the AuNPs clusters. These hot spots, zones of pronounced local field enhancement due to the plasmonic coupling[52], facilitated the enhancement of the MBA Raman intensity (as delineated in the scheme, Fig. 2c). These results demonstrate that the controlled aggregation of AuNPs, guided by liposomes, can be highly effective in enhancing the Raman signal of embedded RRs molecules. Figure 2d, reporting SERS Enhancement Factor (EF) values for 4-MBA SERS tags extrapolated from the literature, compares them to the EF value obtained for 4-MBA embedded in DOPC vesicles upon AuNPs clustering, calculated as reported in the Supplementary Note 2. Remarkably, notwithstanding the simplicity of the synthetic protocol, founded on facile self-assembly steps, the obtained Raman probes display a comparable if not superior efficiency with respect to that of other common Raman probes, synthesized through often complex multistep protocols, or characterized by limited reproducibility and stability.

Characteristics of LipoGold tags: reproducibility, colloidal and functional stability

Since DOPC liposomes provided the highest SERS enhancement, this formulation was then selected for further investigation. Both liposome and 4-MBA concentrations were systematically varied to explore Raman features and maximize SERS signals. Figure 3a, b displays the Raman spectra obtained for DOPC(MBA)-AuNPs for varying vesicle concentrations (Fig. 3a) and varying 4-MBA content within the vesicles (Fig. 3b). It is remarkable that in both cases SERS enhancement trends were not monotonous, as AuNPs/vesicles ratio or 4-MBA concentration were increased. This effect originates in the subtle mechanistic details of AuNPs-lipid vesicles interaction, elucidated in recent studies[41,44,53] and further discussed in Supplementary Fig. 12. However, with the insights gained from this understanding, it was possible to inform the design of LipoGold tags, by tuning and controlling the aggregation of AuNPs on 4-MBA-loaded DOPC vesicles. This optimization included the selection of the balance between RRs amount, liposome concentration, particle aggregation extent, and resulting SERS signal. Eventually, the best outcomes were observed for a 1.2 nM liposomal concentration and a 1% MBA content. Interestingly, as

https://doi.org/10.1038/s41467-024-52205-9

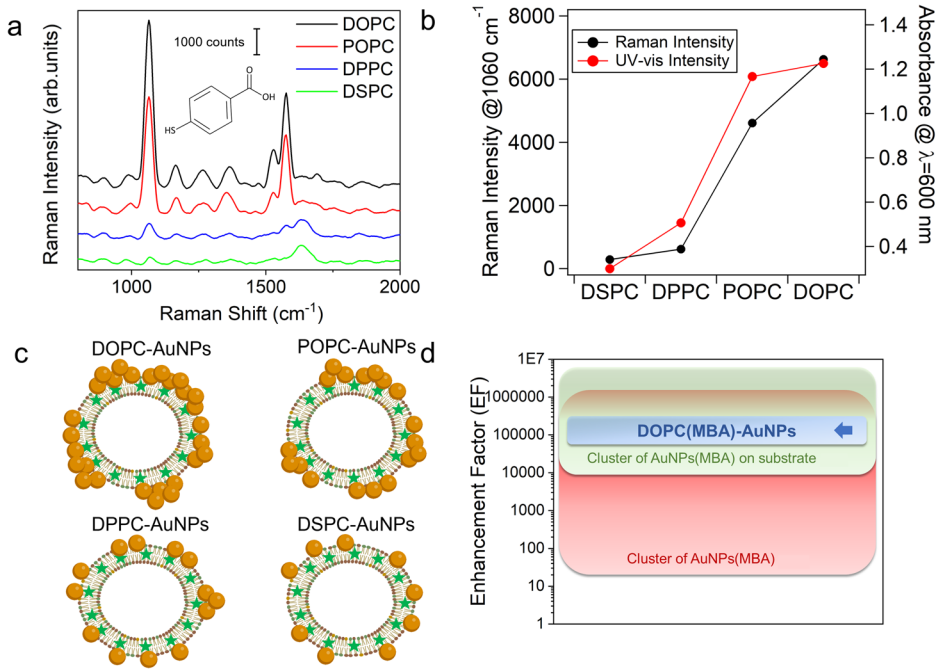

Fig. 2 | SERS signal as a function of membrane rigidity of liposomes. Evaluation of the Raman-SERS and plasmonic properties of LipoGold Tags prepared with four different liposomes' types (DSPC, DPPC, POPC and DOPC). **a** Raman-SERS spectra acquired for different kinds of liposomes (DSPC, DPPC, POPC, and DOPC) with 4-MBA molecules embedded in the bilayer. Excitation wavelength: 638 nm; accumulation time: 60 s; number of acquisitions: 2; objective magnification: 10x. **b** Comparison between the Raman Intensity at 1060 cm^{-1} and UV-Vis signal at 600 nm. **c** Graphical representation of the different interactions between AuNPs and various types of liposomes (DOPC, POPC, DPPC, DSPC). **d** Average enhancement factors (EFs) for clusters of colloidal AuNPs conjugated with 4-MBA (red shaded area) from the literature[28,64,65]); cluster of colloidal AuNPs conjugated with 4-MBA and immobilized onto different substrates (green shaded area) from the literature[66,67,68]); and cluster of colloidal AuNPs interacting with liposome DOPC(MBA) (blue shaded area) presented in this work. Source data are provided as a Source Data file.

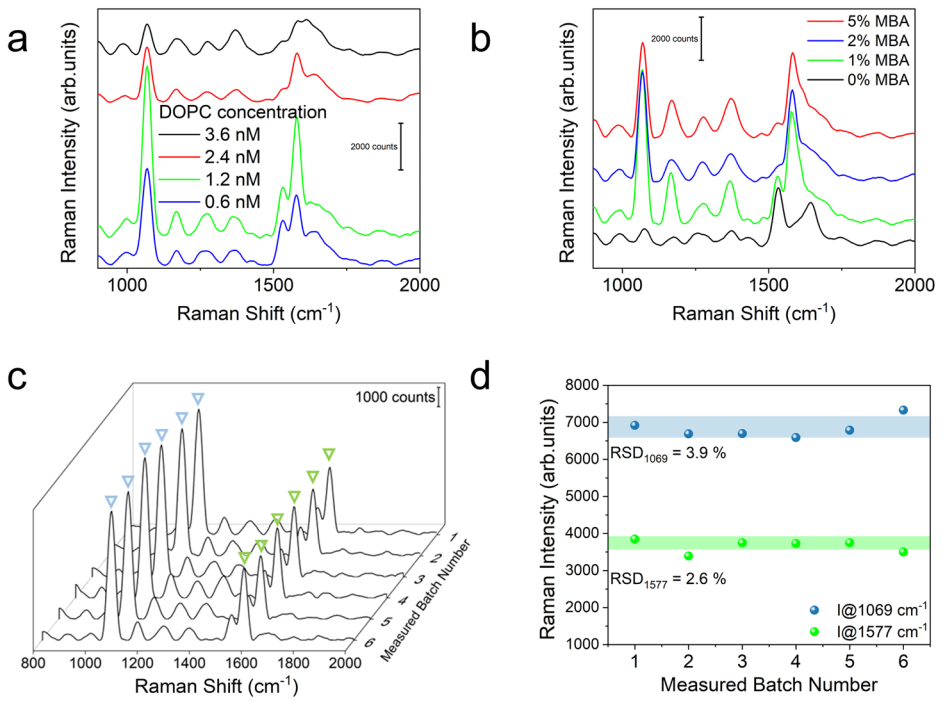

Fig. 3 | Effect of RR concentration on SERS signal and reproducibility of LipoGold tags. Optimization of the synthetic parameters in terms of Raman-SERS performances, reproducibility, colloidal, and functional stability. **a** Raman-SERS spectra of AuNPs interacting with liposome dispersion of DOPC(MBA) at different concentrations; (**b**) Raman-SERS spectra of AuNPs interacting with DOPC liposome dispersion with different MBA concentrations; (**c**) Raman-SERS spectra of six different batches of LipoGold tags; (**d**) Batch-to-batch Raman intensity variation for the 1069 cm^{-1} and 1577 cm^{-1} peaks calculated from the Raman-SERS spectra reported in (**c**). Excitation wavelength: 638 nm; accumulation time: 60 s; number of acquisitions: 2; objective magnification: 10x. Source data are provided as a Source Data file.

https://doi.org/10.1038/s41467-024-52205-9

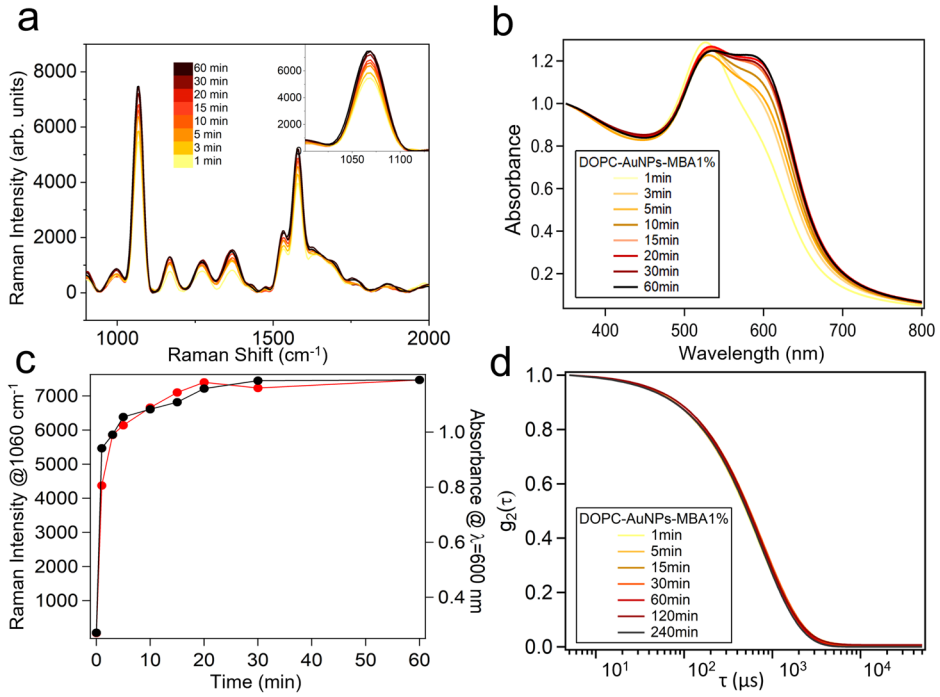

Fig. 4 | Temporal evolution of LipoGold tags. a Time evolution of the Raman and (**b**) UV-visible spectra of DOPC(MBA)-AuNPs LipoGold tags aqueous dispersions; (**c**) Comparison between the time evolution of Raman Intensity at 1060 cm^{-1} and UV-vis signal at 600 nm; (**d**) Time evolution of the DLS autocorrelation functions of DOPC(MBA)-AuNPs LipoGold tags. Excitation wavelength: 638 nm; accumulation time: 60 s; number of acquisitions: 2; objective magnification: 10x. Source data are provided as a Source Data file.

elucidated in the next paragraph, these optimal conditions proved effective for other RRs (see also Supplementary Figs. 13–18), underlying the broad applicability of this strategy, i.e., its potential application for diverse RRs through the same synthetic approach and in the same experimental conditions.

Since one of the major challenges in the fabrication of SERS probes is to maintain batch-to-batch reproducibility, with SERS enhancement varying across different samples, depending on their preparation protocol[25], we evaluated reproducibility, in terms of Raman SERS signals, for six different batches. Figure 3c reports the Raman spectra, while the intensity of the Raman peaks at 1069 and 1577 cm^{-1} is displayed in Fig. 3d. A striking similarity was observed with calculated RSD of the two intensities 3.9% and 2.6%, respectively, thereby demonstrating excellent reproducibility (see Supplementary Fig. 11 for further details on plasmonic and size reproducibility).

We then monitored the characteristics of the probe, in terms of temporal evolution and stability, tracking the time-evolution of both Raman intensities and plasmon absorbance and of the hydrodynamic size of LipoGold tags. Figure 4a displays the progression of Raman intensities, while Fig. 4b illustrates the corresponding evolution of the plasmonic absorption. The time evolution of the Raman enhancement and of the plasmon shift show an abrupt increase upon mixing (Fig. 4c), while a plateau is reached after ~30 min evidencing that most of AuNPs clustering occurs within the first seconds of incubation. Strikingly, the kinetics of Raman enhancement closely resembles the plasmonic variation, implying close and immediate correspondence of the SERS effect with particle aggregation. To verify the colloidal stability of the composites, their dimensional variation was investigated over time via DLS. The normalized autocorrelation functions obtained for DOPC(MBA)-AuNPs adducts are shown in Fig. 4d. The average hydrodynamic diameter (D_h) is stable, as highlighted by the superposition of the autocorrelation functions. The average size obtained by the CONTIN analysis evidenced the presence of hybrids with a characteristic D_h of ~150 nm, consistent with the dimension of vesicles decorated by an AuNP shell. Collectively, these experimental results demonstrate that the interaction of AuNPs with RRs-liposomes lead to the formation of AuNP clusters on the liposomal surface, yielding stable plasmonic and SERS signals after 30 min of incubation. This stability endures over time, even weeks post samples' preparation (see Supplementary Fig. 19).

Functional properties of LipoGold tags: multiplexing

The dependence of colloidal stability, particle aggregation, and SERS reproducibility on the molecular nature of RRs represents one of the main drawbacks in the development of Raman tags based on AuNPs. As a matter of fact, variations in RRs structure affect their density at the NP surface, as well as the NP dispersibility and stability against degradation[25]. For this reason, often SERS probes need specific design for the selected RR, and changes in the RR require significant adjustments of synthetic protocols and conditions[27]. For instance, in the case of AuNP clusters, slight variations in the chemical structure of RR can lead to uncontrolled aggregation due to changes in steric and electrostatic energy contributions. All these hurdles can be circumvented by the presented approach, by encapsulating RRs in the lipid bilayer, thus avoiding effects on the SERS probe colloidal stability and, at the same time, ensuring the effective shielding of the RR from the environment, preserving its optical features.

To prove the versatility of the proposed method, DOPC liposomes embedding three different RRs molecules were prepared and mixed with the AuNPs dispersion (Fig. 5a). More specifically, we prepared and compared DOPC liposomes containing the same amount (1% mol/mol) of MBA, RR2, and RR6. RR2 and RR6 were specifically designed to have bioorthogonal peaks, falling in the biological silent region (1800–2500 cm^{-1}), that is free of background interference thus resulting in a higher signal-to-noise ratio[54]. First, we verified that the probes retained their Raman profiles by acquiring several spectra of the different DOPC(RRs)-AuNPs batches (Fig. 5b), where the characteristic peaks for each tag were highlighted. Then, the effect of liposome and RRs concentration, as well as the colloidal stability and reproducibility of Raman and plasmonic signals, were investigated. As

https://doi.org/10.1038/s41467-024-52205-9

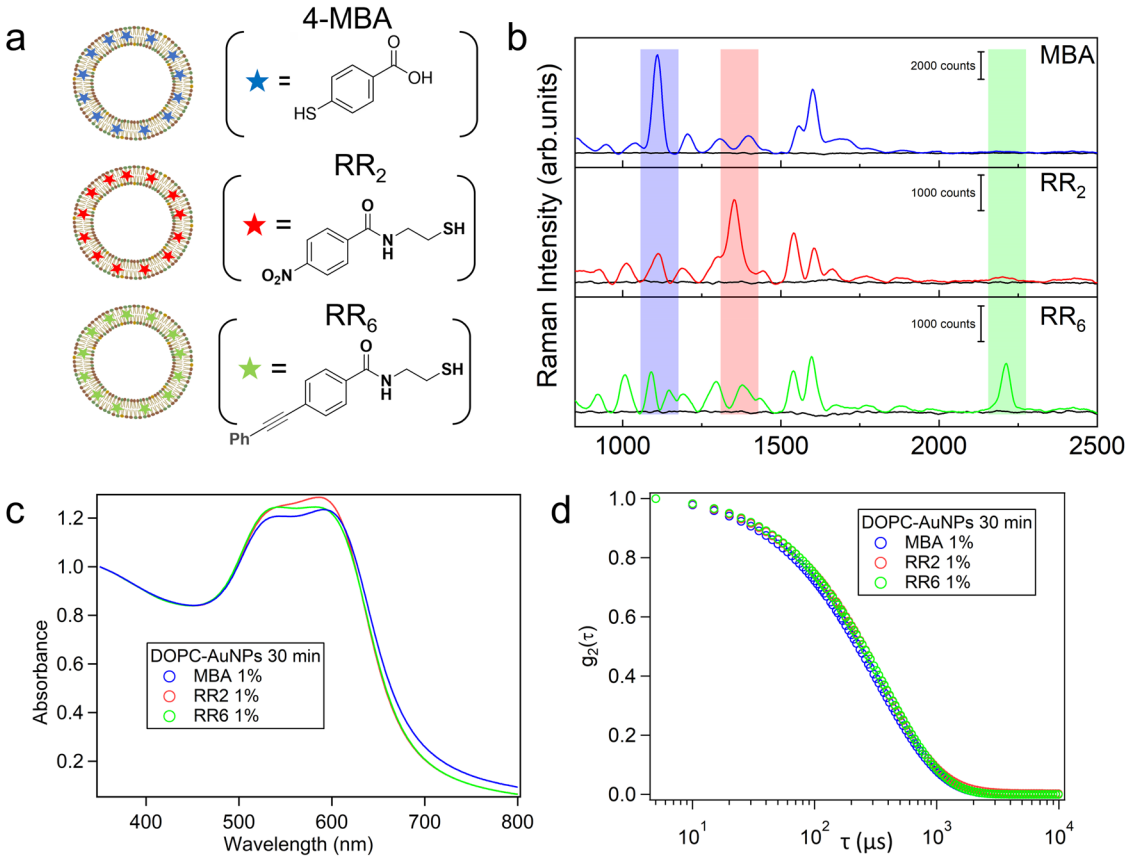

Fig. 5 | Multiplexing properties of LipoGold Tags. a Graphical model representing the three SERS probes constituted by three different RRs; (**b**) Raman-SERS spectra of DOPC(RR)-AuNPs with (colored curves) and without (black curves) the presence of AuNPs. Spectra backgrounds are removed by subtracting the profile of water samples with a 638 nm excitation laser at the same power and same acquisition parameters. Excitation wavelength: 638 nm; accumulation time: 60 s; number of acquisitions: 2; objective magnification: 10x. (**c**) UV-Visible spectra of DOPC(RR)-AuNPs after mixing; (**d**) Dynamic light scattering (DLS) curves obtained by measuring DOPC(RR)-AuNPs after 30 min. of incubation. Source data are provided as a Source Data file.

reported in the Supplementary Figs. 13–18, no significant differences in the preparation protocol were detected when varying the RRs structures. As shown for MBA-containing liposomes, the SERS signal follows the AuNPs clustering-induced plasmonic variations and the interaction can be controlled by varying experimental parameters such as liposome composition and concentration. These results confirm that RR nature doesn't significantly affect the interaction mechanism (see Supplementary Figs. 13–18 for further details). The interaction of DOPC(MBA), DOPC(RR2), and DOPC(RR6) with citrate-capped AuNPs was further compared by monitoring the UV-vis absorption (Fig. 5c) and the hydrodynamic size of the adducts (DLS in Fig. 5d). As shown, while the overall plasmonic variations are slightly affected by the RRs type, probably due to minimal variation in the viscoelastic rigidity of the membrane induced by the different structures of the RRs molecules, the hydrodynamic size of the AuNPs-vesicles adducts is apparently independent (see the remarkable superimposition of the different DLS curves in Fig. 5d). These experimental results demonstrate the robustness and high versatility of this spontaneous aggregation mechanism. Ideally, the same fabrication approach could be employed to form the three SERS probes containing the three different RRs, each bioconjugated with a different antibody, as a straightforward strategy for multiplexing, i.e., detecting separately multiple Raman signals at the same time.

Functional properties of LipoGold tags: bioconjugation

An important advantage of using liposomes as scaffolds for the design of a SERS probe lies in the inherent facile functionalization of the system, which can be simply achieved by including functional or reactive lipids in the liposomal formulation[55]. Depending on specific targeting requirements and characteristics of the target cells or tissues, several functionalization mechanisms can be harnessed. These include ligand-receptor bindings, electrostatic interactions, click chemistry, and antibody conjugations. Most of these approaches leverage the chemical groups that liposomes expose toward the external milieu and that can be systematically introduced in the vesicle preparation with the use of reactive lipids. To this end, we included a pegylated phospholipid with a reactive carboxylic acid moiety (1,2-dioleoyl-sn-glycero-3-phosphoethanolamine-N-[carboxypolyethylene glycol)-2000] sodium salt, DOPE-PEG) into the liposomal membrane. As reported in Fig. 6a, activation of the carboxylic acid moieties leads to the formation of peptide bonds with antibodies. To verify successful bio-coupling, we functionalized DOPC(MBA)-PEG-AuNPs hybrids with fluorescent antibodies (see Methods for details) and we validated the successful functionalization by FCS. This technique involves collecting the temporal fluctuation of the fluorescence intensity. The autocorrelation function of the fluorescence intensity (G(τ)) provides information about the self-diffusion coefficient of fluorescently labeled colloidal objects. As shown in Fig. 6b, the decay time (τ) increases after the functionalization, indicating that the diffusion coefficient of the antibody decreases compared to the free antibody and confirming successful functionalization (see Supplementary Fig. 20 and Supplementary Note 3 for detailed FCS curves analysis).

To assess the targeting ability of antibodies after their conjugation to LipoGold tag, we performed a proof-of-concept SERS experiment in

https://doi.org/10.1038/s41467-024-52205-9

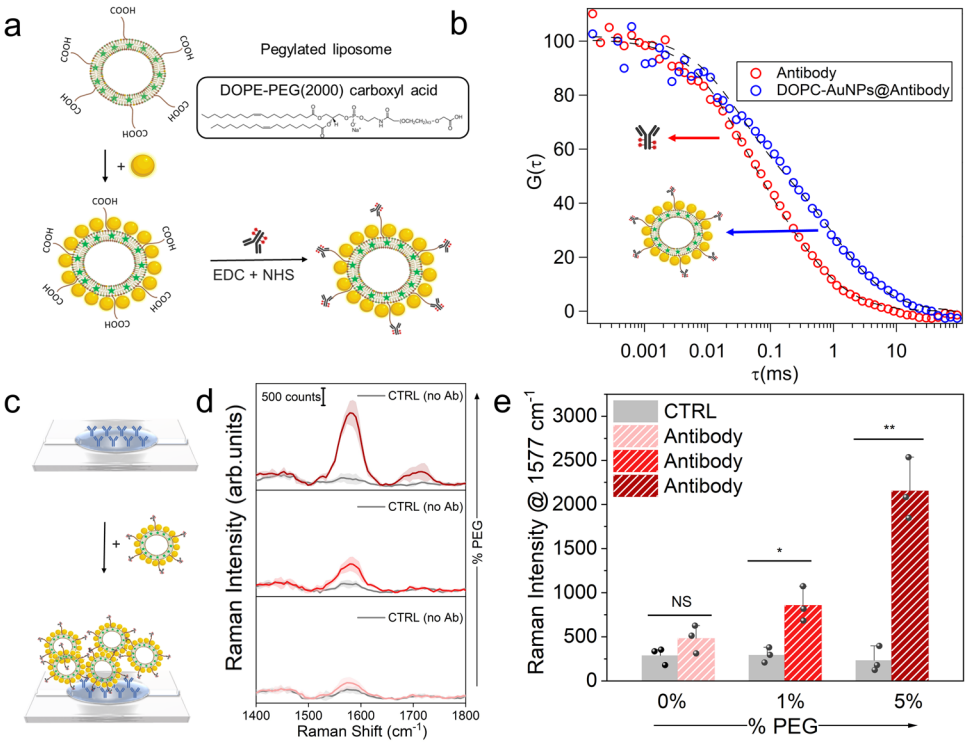

Fig. 6 | Bioconjugation of LipoGold tags. a Graphical scheme reporting the functionalization protocol of liposomes-AuNPs surface with antibodies, exploiting the EDC/NHS coupling mechanism; (**b**) Fluorescence correlation spectroscopy (FCS) measurements of antibodies (Ab(I)) and DOPC-AuNPs@antibody conjugates; (**c**) Graphical scheme reporting the principle of coupling between antibodies(II) attached to the glass slide and antibodies(I) conjugated to the AuNPs-liposome surface (Ab(I)-DOPC(MBA)-PEG-AuNPs); (**d**) Mean Raman-SERS spectra of liposomes with 0%, 1%, and 5% PEG molecules with (red curves) and without (gray curves) antibodies attached to the surface of the glass slide through a sandwich-like immunoassay. Excitation wavelength: 532 nm; accumulation time: 60 s; number of acquisitions: 2; objective magnification: 10x. Data are presented as mean values ± SD. **e** Raman intensity at 1577 cm^{-1} for each sample at different quantities of PEG, with and without antibodies. Data are presented as mean values ± SD. (N_{total} is the number of the replicates (=3); a two-sided student's t-test was performed, with NS > 0.05; *$p < 0.05$; **$p < 0.01$; ***$p < 0.001$). Source data are provided as a Source Data file.

a sandwich-like arrangement. To this end, we first verified that the characteristic Raman signals were still distinguishable after functionalization with primary antibodies, Ab(I) (Supplementary Figs. 21 and 22). Then, the tagging properties of the Ab(I)-DOPC(MBA)-PEG-AuNPs were evaluated in a primary(I)-secondary(II) antibody recognition immunoassay. For this purpose, antibody(II)-modified glass substrates were prepared (see Fig. 6c) and incubated with the Ab(I)-DOPC(MBA)-PEG-AuNPs bioconjugate probe. The Ab(I) concentration was kept constant during the coupling step, while the PEG concentration was increased from 0% (control) to 5%. Raman SERS spectra were then acquired at random single points to attest the presence of SERS probe as a function of PEG content directly related to Ab(I) content. For the PEG levels tested (1% and 5%), the raw spectra showed MBA peaks at 1577 cm^{-1}, confirming that the biorecognition behavior of Ab(I) was preserved even when conjugated to DOPC(MBA)-AuNPs (Fig. 6d, e). Moreover, increasing amounts of PEG molecules, and thus of antibodies conjugated to the liposomal surface, led to an enhancement of the Raman intensity of the MBA peak at 1577 cm^{-1}, while no relevant signals were detected in absence of antibodies (Fig. 6e). This confirmed that SERS probes were not non-specifically assembled onto the substrate when no PEG molecules (and therefore no antibodies) were exposed. These results support the potential of such SERS-based tags as probes for the quantitative detection of analytes in liquid samples.

In vitro tests on LipoGold tags targeting cells

In vitro experiments were performed to evaluate the possibility of using AuNPs-liposomes adducts to label analytes even in heterogeneous and complex systems, such as cell cultures. For this study, probes composed of AuNPs self-assembled on DOPC-5%PEG(RR6) liposomes were chosen (LipoGold(RR6)), since the characteristic peak of RR6 falls in the biologically silent region, where no peaks attributable to cells are visible[54]. The PEG pendant moieties were modified with Cholera Toxin Subunit B-FITC™ (CT-B), a fluorescently labeled protein that specifically binds the GM1 ganglioside, a component of the plasma membrane. Similar to the strategy reported in the previous paragraph, here the biofunctionalization protocol is based on standard amide bond formation and can therefore be exploited to conjugate any capturing agents exposing amino functionalities. SHSY-5Y fixed cell cultures were incubated with CT-B-LipoGold(RR6) for 90 min and then thoroughly washed with water to remove unbound SERS probes. Cell incubation with free CT-B and LipoGold(RR6)dispersions were performed as control experiments. For this experiment, cells were previously fixed to avoid non-specific endocytosis, mitosis, and even plasma membrane remodeling during the relatively long incubation (90 min).

As shown in the confocal images in Fig. 7a, the intense green fluorescent signal from FITC was observed on the surface of cells incubated either with the free tag CT-B-LipoGold(RR6), while no signal was observed when incubated with bare SERS probes LipoGold(RR6). This demonstrated the high selectivity and specificity of the liposome-based SERS nanoprobes even when working with complex matrices. The bright field image (Fig. 7b) displays the analyzed cells and their corresponding SERS map. The green rectangle represents the area scanned with Raman confocal microscopy used to build the map by exploiting the SERS intensity of the peak located at 2210 cm^{-1}, in the biological silent region. As an example, Fig. 7c reports SERS spectra collected from three different points on the map. The color of each

https://doi.org/10.1038/s41467-024-52205-9

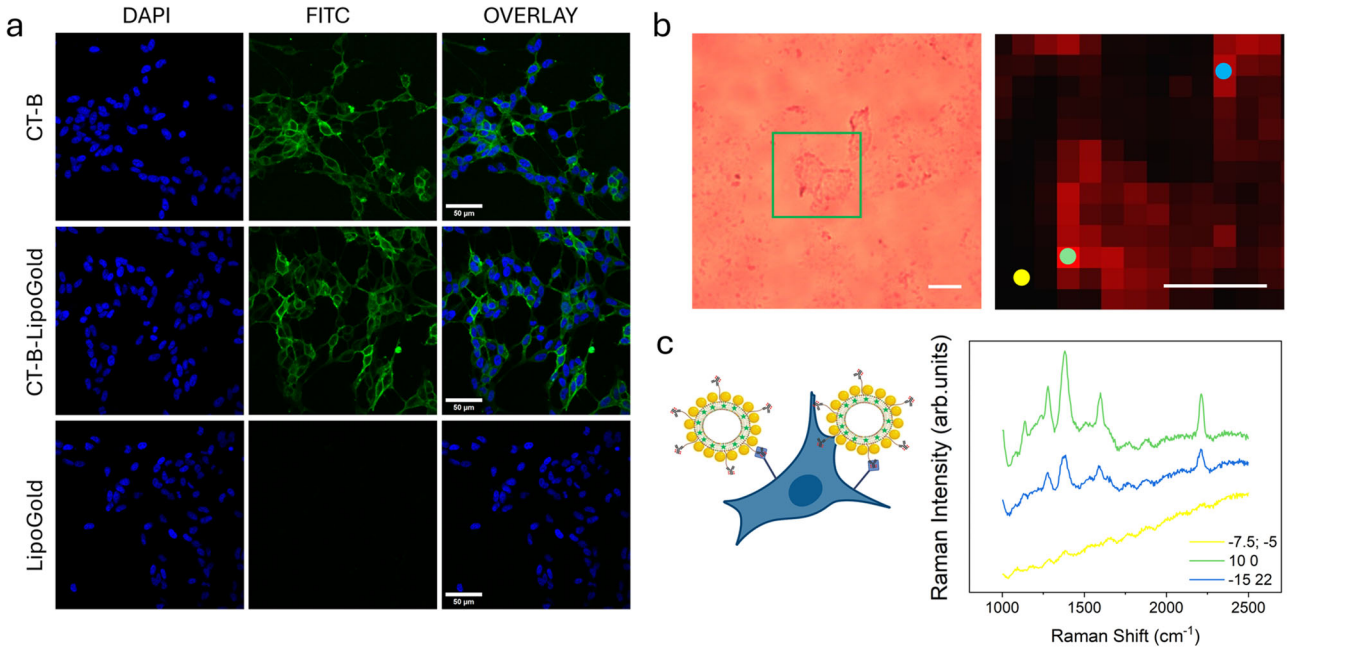

Fig. 7 | In vitro targeting of cells with LipoGold tags. a Representative confocal microscope images of SHSY-5Y cells incubated with free CT-B, CT-B- LipoGold, and bare LipoGold. Scale bar is 50 µm in all cases; (**b**) Left panel shows the bright field image of the analyzed SH-SY5Y cells treated with LipoGold(RR6) for 90 min. The green rectangle represents the scanned area with Raman confocal microscopy. Right panel shows the SERS map generated exploiting the intensity at 2210 cm^{-1}. Scalebar is 10 µm in all cases. Measurements were performed with the following parameters: laser 638 nm, 20 mW laser power, 30 s acquisition time, 1 accumulation, 272 data points, Y step 2 µm and X step 3 µm, objective magnification: 60x. **c** Representative SERS spectra acquired from cells in (**b**). Yellow spectrum corresponds to $x = -7.5$ µm, $y = -5$ µm (yellow dot); blue spectrum corresponds to $x = -15$ um, $y = 22$ µm (blue dot); green spectrum corresponds to $x = 10$ um; $y = 0$ µm (green dot). The representative microscopy experiments have been repeated two times. Source data are provided as a Source Data file.

spectrum corresponds to the respective dot shown in Fig. 7b. Other SERS maps are reported in Supplementary Fig. 24, revealing the possibility to identify cell morphology by mapping the localization of the strong narrow peak characteristic of RR6 when NPs-liposomes tags are bioconjugated with CT-B.

LipoGold SERS detection of disease-related alterations of GM1

Finally, in a diagnostic experiment aimed at detecting GM1 alterations, we leveraged the SERS signal variations in fibroblasts obtained from skin biopsies of an infantile GM1 gangliosidosis patient and a healthy donor. The defining cellular characteristic of this metabolic disorder is the intracellular accumulation of GM1 ganglioside within lysosomes[56]. Previous studies have demonstrated the effectiveness of distinguishing GM1 levels in fibroblasts from affected and unaffected individuals using CT-B coupled with flow cytometry[57,58]. This latter approach was used as a benchmark to assess the efficacy and sensitivity of functionalized LipoGold/SERS in comparison to fluorescence-based methods. To this end, LipoGold probes were functionalized with CT-B, following the same protocol outlined in the previous paragraph. In contrast to the experiment reported in Fig. 7, fixed cells were permeabilized to enable the detection of intracellular GM1, since surface labeling alone was previously demonstrated to be not sufficient to detect differences[58]. Fibroblasts from patient and healthy donor were then incubated with equivalent amounts of CT-B either in free form or coupled to LipoGold, and the fluorescence intensity values per cell were subsequently measured with flow cytometry. The measured side scatter intensities indicate a higher degree of complexity (i.e., granularity) inside control cells incubated with CT-B-LipoGold with respect to cells incubated with CT-B alone (Fig. 8a), possibly related to the efficient penetration of CT-B-LipoGold particles inside the permeabilized cells. Approximately the same two-fold increase in fluorescence intensity, correlated to the intracellular amounts of GM1, was found in patient cells with respect to wild-type, either when incubated with free CT-B or with CT-B-LipoGold (Fig. 8b). Although encouraging, these data alone could not however demonstrate that the conjugation step between CT-B and LipoGold was stable.

The same treated samples were finally analyzed with a confocal Raman microscope and Raman-SERS spectra from 10 individual cells per sample were acquired (Supplementary Fig. 23). The calculated averaged spectra distinctly delineate the emergence of SERS signals associated with MBA at 1069 and 1577 cm^{-1}, exclusively in the presence of LipoGold (red and gray lines in Fig. 8c). Remarkably, the intensity of the Raman peaks was observed to be up to 7-fold higher for the patient sample compared to the healthy control counterpart (Fig. 8d). In comparison, with flow cytometry the fluorescence signal was found to increase by 2-fold. Taken together, the flow cytometry and Raman microscopy data demonstrate not only that the LipoGold particles can access the interior of the permeabilized cells, but also that the functionalized particles are structurally stable and that the binding between the CT-B and the Raman probe is retained. Moreover, the strongly amplified distinction in Raman signal intensities between healthy and pathological samples due to the LipoGold probes offers a valuable and highly sensitive tool for the diagnosis of diseases characterized by alterations of GM1 levels (GM1 gangliosidosis, Niemann Pick C, Alzheimer's and others[59]), which could in principle be extended, using the relative specific probes, to the diagnosis and follow-up of any other disease characterized by subtle changes in specific metabolites levels.

In summary, we have introduced a simple synthetic route to create SERS probes (LipoGold tags) of remarkable efficiency, versatility, and facile functionalization. Our approach harnesses the spontaneous association of citrate-capped AuNPs on lipid vesicles. We showed that AuNPs aggregation on lipid bilayers encapsulating Raman reporters leads to an enhancement of their Raman signals by several orders of magnitude. This strategy holds the promise to overcome the common challenges in SERS probe fabrication, specifically addressing synthetic

https://doi.org/10.1038/s41467-024-52205-9

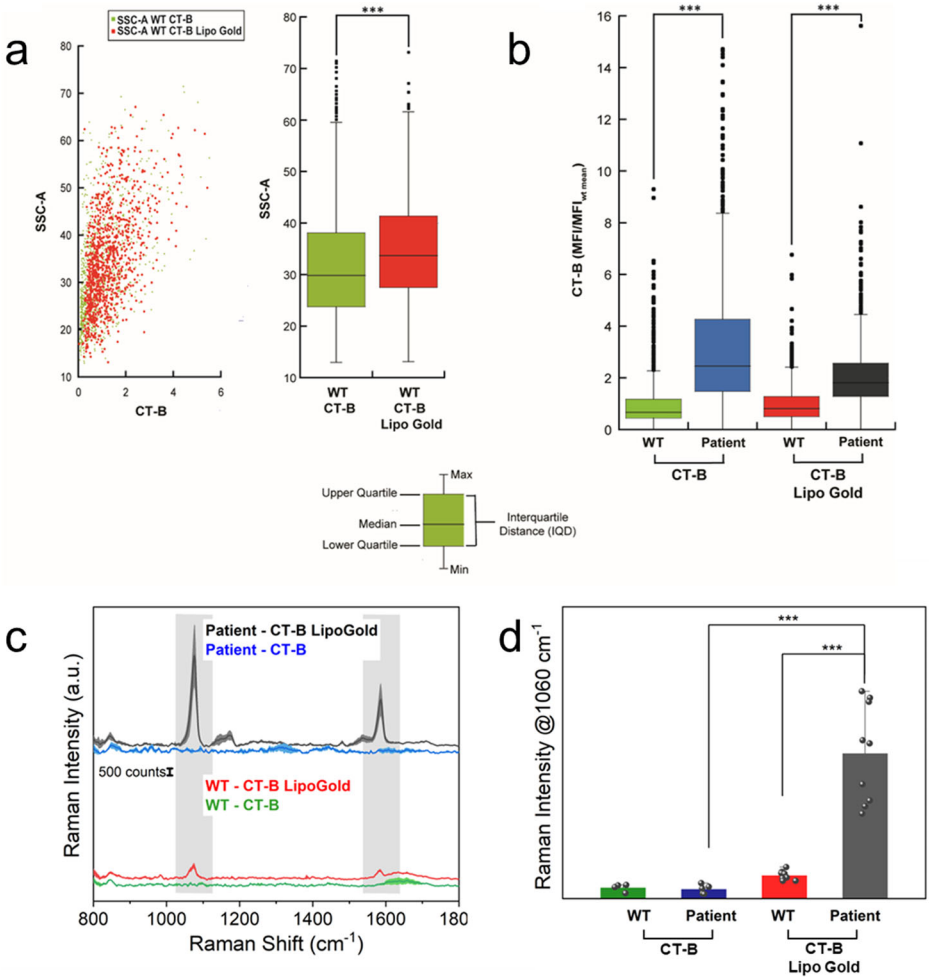

Fig. 8 | Detection of GM1 alterations using LipoGold tags. a FACS analysis of lymphocytes from WT and from patient affected by juvenile GM1 gangliosidosis. Lymphocytes were fixed and incubated for 45 min with 5 μg/mL of CT-B or 5 μg/mL of CT-B LipoGold, previously dissolved in distilled H_2O. FACS analysis showed a significant variation in the SSC-A of WT cells labeled with CT-B-LipoGold compared with WT marked with CT-B. **b** MFI/MFIWT mean values are obtained by dividing the MFI of a distribution by the mean MFI obtained from the controls. MFI/MFIWT mean values increase significantly in patients compared to WT control. N_{total} is the number of replicates (=3), 1000 cells were analyzed. Data are presented as mean values ± SD. A two-sided student's t-test was performed with NS > 0.05; $^{*}p < 0.05$; $^{**}p < 0.01$; $^{***}p < 0.001$. Median: the data value located halfway between the smallest and largest value. Upper Quartile: the data value located halfway between the median and the largest data value. Lower Quartile: the data value located halfway between the median and the smallest data value. Interquartile Distance (IQD): the distance between the Upper and the Lower Quartiles. Max: maximum value. Min: minimum value. **c** Averaged Raman-SERS spectra acquired for WT in the presence of CT-B (green line, $n = 4$) and CT-B-LipoGold (red line, $n = 9$), and averaged Raman-SERS spectra acquired for patient sample in the presence of CT-B (blue line, $n = 5$) and CT-B-LipoGold (gray line, $n = 9$). Data are presented as mean values ± SD. Excitation wavelength: 638 nm; accumulation time: 120 s; number of acquisitions: 2; objective magnification: 10x. **d** Histogram showing the quantitative values of Raman intensity at 1060 cm^{-1}. Error bars are standard deviations ($n = 4$, 9, 5, 9, respectively; a two-sided student's t test was performed, with NS > 0.05; $^{*}p < 0.05$; $^{**}p < 0.01$; $^{***}p < 0.001$). Source data are provided as a Source Data file.

simplicity, reproducibility, and optical and colloidal stability. We monitored the Raman signal in parallel with plasmonic variations of LipoGold tags, as lipid composition and liposome and RRs concentration were varied, highlighting a striking correspondence between spontaneous AuNPs clustering and Raman intensity enhancement. LipoGold tags were comprehensively characterized from a structural point of view and their colloidal and optical stability monitored over several weeks. Significantly, the versatility of our approach remains unaltered even when the molecular structures of Raman reporters differ, thereby extending its applicability to multiplexing.

Furthermore, the easy tunability of the liposomal surface provides a platform for bioconjugation with antibodies, enabling precise targeting specificity. This versatility is demonstrated by the specific detection of intracellular alterations in GM1 levels. This ensemble of features not only highlights the adaptability of our approach for diagnosing diseases characterized by GM1 alterations but also expands its potential for diverse pathologies and applications.

Overall, our method lays the basis for pioneering synthetic protocols, marking a transformative shift in the field of SERS nanoprobes. By offering thermodynamic control over both structure and colloidal characteristics and potential for bioconjugation, this approach can represent a milestone in the field of AuNP cluster-based SERS nanoprobes.

Methods

All experiments on biological materials were performed in accordance with the ethical standards of the institutional research committee and with the 1964 Helsinki Declaration and its later amendments. In keeping with ethical guidelines, all fibroblasts cell lines obtained from skin biopsy were stored and anonymized to be used only for research

purposes after written informed consent of the patients (and/or their family members) was obtained.

Chemicals

Tetrachloroauric (III) acid (99.9%), trisodium citrate dihydrate (99.9%), N-(3-Dimethylaminopropyl)-N-ethylcarbodiimide hydrochloride (EDC; 99.9%); N-Hydroxysuccinimide (NHS; 99.9%) were purchased from Sigma-Aldrich (St. Louis, MO). 1,2-Dioleoyl-sn-glycero-3-phosphocholine (DOPC) (99%), 1,2-dioleoyl-sn-glycero-3-phosphoethanolamine-N-[carboxypolyethylene glycol)-2000] sodium salts (DOPE-PEG) (99%), 1-palmitoyl-2-oleoylsn-glycero-3-phosphocholine (POPC) (98%), 1,2-distearoyl-sn-glycero-3- phosphocholine (DSPC) (99%) and 1-dipalmitoyl-sn-glycero-3-phosphocholine (DPPC) (99%) were provided by Avanti Polar Lipids. Milli-Q-grade water was used in all preparations. THY-1 SC-9163 rabbit polyclonal IgG 200 ug/ml (AbI); Cholera Toxin B subunit, FITC conjugate (CT-B, Sigma-Aldrich Merck). *RRs*: 4-Mercaptobenzoic acid (4-MBA; 99.9%). *For RRs synthesis*: 1-[Bis(dimethylamino)methylene]-1H-1,2,3-triazolo[4,5-b]pyridinium 3-oxid hexafluorophosphate (HATU; 97%), trifluoroacetic acid (TFA; 99.9%), triphenyl- methanol, triisopropylsilane (TIPS; 98%), 2-thioethylamine (99%), benzoic acids and all organic solvents were purchased from Merck. Chemical compounds are named as follows: RR2: 4-nitro-N-(2-mercaptoethyl)benzamide; RR6: 4-(phenylethynyl)-N-(2-mercaptoethyl)benzamide. DMEM/F12 medium, FBS, penicillin/streptomycin solution, Opti-MEM were purchased from ThermoFisher Scientific.

Preparation of liposomes

To prepare liposomes containing RRs, the appropriate amounts of lipids (DOPC, POPC, DPPC, and DSPC) and of RRs were dissolved in chloroform/methanol (3/1), and the solvent evaporated under a stream of nitrogen and overnight vacuum drying. The lipid-RR film was then hydrated with warm (50 °C) Milli-Q water by vigorous vortex mixing, resulting in a final 4 mg/ml lipid concentration. The resultant multilamellar vesicles (MVLs) were subjected to 10 freeze–thawing cycles and extruded 10 times through two stacked polycarbonate membranes with a 100 nm pore size. This process yielded unilamellar vesicles with a narrow and reproducible size distribution. The extrusion was performed with the Extruder (Lipex Biomembranes, Vancouver, Canada) through Nuclepore membranes.

Synthesis of AuNPs

Anionic gold nanospheres of 12 nm in size were synthesized according to the Turkevich-Frens method[60,61]. Briefly, 20 mL of a 1 mM $HAuCl_4$ aqueous solution was brought to boiling temperature under constant and vigorous magnetic stirring. 2 mL of 1% citric acid solution was then added and the solution was further boiled for 20 min until it acquired a deep red color. The AuNPs dispersion was then slowly cooled down to room temperature.

Preparation of LipoGold tags

AuNPs-liposome hybrids (LipoGold tags) were synthesized by incubating freshly prepared Turkevich-Frens AuNPs dispersion (300 µL 6 nM) with an appropriate amount of 30 nM liposome dispersions, obtaining the following final liposome concentrations: 0.5, 0.8, 1, 2, and 5 nM.

Antibody functionalization and sandwich-like assay

Antibodies-bioconjugates were prepared starting from the as-prepared NPs-liposomes constructs reported in "Methods" section. Incubation was performed in water for 1 h at room temperature after activation with 0.4 mM EDC and 0.1 mM NHS (final concentration) for 30 min. An amount of 6 µL of 500 µg/mL stock solution of antibody was added to 300 µL of NPs-hybrid conjugates, resulting in a 50 times dilution (0.1 mg/mL antibodies solution). After the NPs-bioconjugation, the glass slide was functionalized following an optimized protocol, where 30 µl of Ab(II) 200 ug/ml were fluxed within the chamber and incubated for 4 min. Then, the substrate was rinsed thrice with distilled water, followed by a second incubation with 30 µl of Ab(I)-NPs-liposomes conjugates for 3 min. Substrate was rinsed again thrice with distilled water to remove unbound probes.

UV-vis spectroscopy

UV-vis spectra were recorded with a Cary 3500 UV-vis spectrophotometer.

Dynamic light scattering (DLS)

DLS measurements at $\theta = 90°$ and the ζ-potential determination were performed using a Brookhaven Instrument 90 Plus (Brookhaven, Holtsville, NY). Each measurement was the average of 5 repetitions of 1 min each, and measurements were repeated 3 times. The autocorrelation functions (ACFs) were analyzed through a cumulant fitting stopped at the second order for samples characterized by a single monodisperse population, allowing an estimate of the hydrodynamic diameter of particles and the polydispersity index. For polydisperse samples, the experimental ACFs were analyzed through Laplace inversion according to the CONTIN algorithm. ζ-potentials were obtained from the electrophoretic mobility u according to Helmholtz −Smoluchowski equation) × µ (1) where η is the viscosity of the medium and ε is the dielectric permittivity of the dispersing medium. The ζ-potential values are reported as averages from 5 measurements.

Fluorescence correlation spectroscopy (FCS)

FCS measurements were performed with a Leica TCS SP8 confocal microscope (Leica Microsystems GmbH, Wetzlar, Germany) equipped with a PicoQuant FCS modulus (PicoQuant, Berlin, Germany). Measurements were performed using a 63× water immersion objective, the Ab(I)-DOPC(MBA)-AuNPs was excited using a 488 nm-laser line of an Ar laser, and the fluorescence intensity was acquired using a Hybrid SMD detector in the 498–530 nm range. An aqueous solution of Rhodamine 110 was employed for calibration. In FCS the time fluctuation of the fluorescence intensity of a fluorescent species diffusing inside and outside the detection volume is analyzed to calculate the autocorrelation function of the fluorescence intensity G(τ). If the detection volume is well described by a 3D-ellipsoidal Gaussian shape and three-dimensional Brownian diffusion is the only phenomenon observed, for one diffusing species, the FCS curves can be analyzed according to:

$$G(\tau) = 1/N\left(1+\frac{\tau}{\tau D}\right)^{-1}\left(1+\frac{\tau}{S^2\tau D}\right)^{-1/2} \quad (1)$$

with N being the average number density of the fluorescent objects, S the structural parameter of the detection volume ($S = z_0/w_0$ with w_0 and z_0 lateral and axial parameters, determined through calibration), and τ_D the decay time[62].

Cryo-transmission electron microscopy (Cryo-TEM)

3 µL of each sample were applied on glow discharged Quantifoil Cu 300 R2/2 grids. The samples were frozen in liquid ethane using an FEI Vitrobot Mark IV (Thermo Fisher Scientific) instrument. Excess liquid was removed by blotting for 1 s using filter paper under 100% humidity and 10 °C. Cryo-EM data were collected at the Florence Center for Electron Nanoscopy (FloCEN), University of Florence, on a Glacios (Thermo Fisher Scientific) instrument at 200 kV equipped with a Falcon III detector operated in the counting mode. Images were acquired using EPU software with a physical pixel size of 2.5 Å and a total electron dose of ~50 e − /Å2 per micrograph.

Cell culture
Human SH-SY5Y neuroblastoma cells (A.T.C.C., USA) and primary fibroblasts were cultured in Dulbecco's Modified Eagle's Medium (DMEM) (ThermoFisher Scientific, USA) F-12 Ham (1:1) supplemented with 10% Fetal Bovine Serum (FBS), 1.0 mM glutamine and 1% penicillin/streptomycin solution in a 5% CO_2 humidified atmosphere at 37 °C and grown until 80% confluence. The provided fibroblasts[57] are anonymised and used only for research purposes.

Confocal microscopy imaging
Living SH-SY5Y cells were plated in 12-well plates containing glass coverslips and incubated in a single step with DAPI, CT-B, and/or LipoGold 1 nM for 90 min at 37 °C in the incubator, and rinsed with PBS. The analysis of blue and green fluorescence was performed on a Nikon Eclipse TE300 C2 confocal laser scanning (CLSM) (Nikon, Japan) equipped with a Nikon a 100× Plan Apo lambda oil immersion objective after excitation with Coherent CUBE (diode 405 nm) and Melles Griot (Argon 488 nm) lasers, respectively. Emission filters for imaging were 452/45 nm and 514/30 nm. Optical sections (1024 × 1024 pixels) at the cell median planes were taken and analyzed using ImageJ software (National Institutes of Health, Bethesda, MD, USA). All settings, including pinhole diameter, detector gain, and laser power were kept constant for each analysis.

Flow cytometry analysis
Fibroblasts from the wild-type (WT) control and from patients were plated in 12-well plates at a 30,000 cells/well density. Twenty-four hours after plating, the cells were harvested and washed with PBS. A BD Cytofix/CytopermTM Fixation/Permeabilization Solution kit (BD Biosciences, Lake Franklin, NJ, USA) was used for fixation according to the manufacturer's instructions. Then fibroblasts were incubated for 45 min at room temperature with 5 μg/mL of CT-B or 5 μg/mL of CT-B LipoGold, previously dissolved in distilled H_2O. After washing with distilled H_2O, the samples were analyzed on a Accuri-C6 flow cytometer (BD Biosciences, Lake Franklin, NJ, USA). Data were analyzed using the free Flowing software (Cell Imaging and Cytometry Core, Turku Bio-science Centre, Turku, Finland). The fibroblasts were identified by side-scattered and forward-scattered light. The GM1 levels were quantified by the median fluorescence intensity of the cellular population.

Confocal Raman microscopy
Raman spectra were collected with a conventional micro-Raman setup (XploRA PLUS Confocal Raman Microscope, Horiba, Kyoto, Japan), equipped with 532, 633, and 785 nm lasers (Coherent, Santa Clara, CA, USA) and a spectrometer with a focal length of 500 mm, equipped with a 600 and 1200 lines/mm grating. The incident laser power on the sample was about 20 mW. The scattered light was detected by a CCD camera operating at about 350 K. Raman-SERS spectra were recorded in the wavenumber range of 800–2500 cm^{-1}, the acquisition time was 60 s and the measurements were repeated twice for spectral averaging. To avoid spurious signals, calcium fluoride Raman slides (CaF_2, Crystran, Dorset, UK) were used as substrates. To extract the Raman signal of interest, fluorescence and background signals were subtracted from the acquired raw spectra through Vancouver Raman Algorithm, a dedicated software for automatic autofluorescence background subtraction for Raman spectroscopy[63]. Data was further analyzed with Origin software.

Statistics and reproducibility
Statistical analyses were conducted with OriginPro 2020b and GraphPad. The statistical analysis methods were described in the figure legends. No data were excluded from the analyses. $^{*}p < 0.05$, $^{**}p < 0.01$, $^{***}p < 0.001$, and $^{****}p < 0.0001$ were considered statistically significant.

Reporting summary
Further information on research design is available in the Nature Portfolio Reporting Summary linked to this article.

Data availability
All data supporting the findings of this study are presented in the Article, Supplementary Information, and Source Data file. Data have been also deposited within the public repository https://doi.org/10.6084/m9.figshare.26411992.v1. Source data are provided with this paper.

References

1. Pilot, R. et al. A review on surface-enhanced Raman scattering. *Biosensors* **9**, 57 (2019).
2. Du, Z., Qi, Y., He, J., Zhong, D., Zhou, M. Recent advances in applications of nanoparticles in SERS in vivo imaging. *WIREs Nanomed. Nanobiotechnol.* **13**, https://doi.org/10.1002/wnan.1672 (2021).
3. Langer, J. et al. Present and future of surface-enhanced Raman scattering. *ACS Nano* **14**, 28–117 (2020).
4. Li, L. et al. Near-infrared II plasmonic porous cubic nanoshells for in vivo noninvasive SERS visualization of sub-millimeter microtumors. *Nat. Commun.* **13**, 5249 (2022).
5. Le Ru, C., Blackie, E., Meyer, M., & Etchegoin, P. G. Surface enhanced raman scattering enhancement factors: a comprehensive study. *J. Phys. Chem. C.* **111**, 13794–13803 (2007).
6. Wang, Y., Yan, B. & Chen, L. SERs tags: novel optical nanoprobes for bioanalysis. *Chem. Rev.* **113**, 1391–1428 (2013).
7. Sharma, B. et al. High-performance users substrates: advances and challenges. *MRS Bull.* **38**, 615–624 (2013).
8. Chen, N. et al. Porous carbon nanowire array for surface-enhanced Raman spectroscopy. *Nat. Commun.* **11**, 4772 (2020).
9. Kennedy, D. C., Hoop, K. A., Tay, L., & Pezacki, J. Development of nanoparticle probes for multiplex SERS imaging of cell surface proteins. *Nanoscale* **2**, 1413–1416 (2010).
10. Chen, Z. et al. Multicolor live-cell chemical imaging by isotopically edited alkyne vibrational palette. *J. Am. Chem. Soc.* **136**, 8027–8033 (2014).
11. Zavaleta, C. L. et al. Multiplexed imaging of surface-enhanced Raman scattering nanotags in living mice using noninvasive Raman spectroscopy. *Proc. Natl Acad. Sci. USA* **106**, 13511–13516 (2009).
12. Laing, S., Jamieson, L. E., Faulds, K. & Graham, D. Surface-enhanced Raman spectroscopy for in vivo biosensing. *Nat. Rev. Chem.* **1**, 0060 (2017).
13. Harmsen, S., Wall, M. A., Huang, R. & Kircher, M. F. Cancer imaging using surface-enhanced resonance Raman scattering nanoparticles. *Nat. Protoc.* **12**, 1400–1414 (2017).
14. Zhang, Y., Gu, Y., He, J., Thackray, B. D. & Ye, J. Ultrabright gap-enhanced Raman tags for high-speed bioimaging. *Nat. Commun.* **10**, 3905 (2019).
15. Yarbakht, M. et al. Simultaneous isolation and detection of single breast cancer cells using surface-enhanced Raman spectroscopy. *Talanta* **186**, 44–52 (2018).
16. Fabris, L. SERS tags: the next promising tool for personalized cancer detection? *ChemNanoMat* **2**, 249–258 (2016).
17. Li, M. et al. Alkyne-and nitrile-anchored gold nanoparticles for multiplex SERS imaging of biomarkers in cancer cells and tissues. *Nanotheranostics* **3**, 113–119 (2019).
18. Dallari, C. et al. Multilayered bioorthogonal SERS nanoprobes selectively aggregating in human fluids: a smart optical assay for β-amyloid peptide quantification. *ACS Sens.* **8**, 3693–3700 (2023).
19. Dallari, C. et al. Gold nanostars bioconjugation for selective targeting and SERS detection of biofluids. *Nanomaterials* **11**, 1–16 (2021).

20. Li, M., Kang, J. W., Sukumar, S., Dasari, R. R. & Barman, I. Multiplexed detection of serological cancer markers with plasmon-enhanced Raman spectro-immunoassay. *Chem. Sci.* **6**, 3906–3914 (2015).
21. Harmsen, S. et al. Rational design of a chalcogenopyrylium-based surface-enhanced resonance Raman scattering nanoprobe with attomolar sensitivity. *Nat. Commun.* **6**, https://doi.org/10.1038/ncomms7570 (2015).
22. Lenzi, E., Jimenez de Aberasturi, D. & Liz-Marzán, L. M. Surface-enhanced Raman scattering tags for three-dimensional bioimaging and biomarker detection. *ACS Sens.* **4**, 1126–1137 (2019).
23. Rodal-Cedeira, S. et al. I. An expanded surface-enhanced Raman scattering tags library by combinatorial encapsulation of reporter molecules in metal nanoshells. *ACS Nano* **14**, 14655–14664 (2020).
24. Zhu, J. et al. The functional Fe3O4@SiO2@AuNPs SERS nanomaterials for rapid enrichment and detection of mercury ions in Licorice. *Chemosensors* **10**, https://doi.org/10.3390/chemosensors10100403 (2022).
25. Schumacher, M. et al. Robust encapsulation of biocompatible gold nanosphere assemblies for bioimaging via surface enhanced Raman scattering. *Adv. Opt. Mater.* **10**, https://doi.org/10.1002/adom.202102635 (2022).
26. Taylor, R. W., Esteban, R., Mahajan, S., Aizpurua, J. & Baumberg, J. J. Optimizing SERS from gold nanoparticle clusters: addressing the near field by an embedded chain plasmon model. *J. Phys. Chem. C.* **120**, 10512–10522 (2016).
27. Rodal-Cedeira, S. et al. An expanded surface-enhanced raman scattering tags library by combinatorial encapsulation of reporter molecules in metal nanoshells. *ACS Nano* **14**, 14655–14664 (2020).
28. Zhou, Y. et al. Multiplexed SERS barcodes for anti-counterfeiting. *ACS Appl. Mater. Interfaces* **12**, 28532–28538 (2020).
29. Zhang, A. et al. Exploring the generality of ligands for silica-encapsulated nanoclusters as SERS labels. *J. Colloid Interface Sci.* **635**, 43–49 (2023).
30. Wang, J., Liang, D., Jin, Q., Feng, J. & Tang, X. Bioorthogonal SERS nanotags as a precision theranostic platform for in vivo SERS imaging and cancer photothermal therapy. *Bioconjug. Chem.* **31**, 182–193 (2020).
31. Ip, S. et al. Dual-mode dark field and surface-enhanced Raman scattering liposomes for lymphoma and leukemia cell imaging. *Langmuir* **35**, 1534–1543 (2019).
32. Srivastava, I. et al. Biomimetic surface-enhanced Raman scattering nanoparticles with improved dispersibility, signal brightness, and tumor targeting functions. *ACS Nano* **16**, 8051–8063 (2022).
33. Liu, H., Gao, X., Xu, C. & Liu, D. SERS tags for biomedical detection and bioimaging. *Theranostics* **12**, 1870–1903 (2022).
34. Jeong, J. E. et al. Resonant Raman-active polymer dot barcodes for multiplex cell mapping. *ACS Nano* **17**, 4800–4812 (2023).
35. Lai, Q., Wang, T., Sun, Y. & Aguey-Zinsou, K. F. Rational design of nanosized light elements for hydrogen storage: classes, synthesis, characterization, and properties. *Adv. Mater. Technol.* **3**, 1–43 (2018).
36. Stewart, F. et al. Rational design for the controlled aggregation of gold nanorods via phospholipid encapsulation for enhanced Raman scattering. *ACS Nano* **8**, 5462–5467 (2014).
37. Li, J. et al. A digital single-molecule nanopillar SERS platform for predicting and monitoring immune toxicities in immunotherapy. *Nat. Commun.* **12**, 1087 (2021).
38. Lim, D. K. et al. Highly uniform and reproducible surface-enhanced Raman scattering from DNA-tailorable nanoparticles with 1-Nm interior gap. *Nat. Nanotechnol.* **6**, 452–460 (2011).
39. Sugikawa, K., Kadota, T., Yasuhara, K. & Ikeda, A. Anisotropic self-assembly of citrate-coated gold nanoparticles on fluidic liposomes. *Angew. Chem. - Int. Ed.* **55**, 4059–4063 (2016).
40. Wang, Z. et al. Fluidity-guided assembly of Au@Pt on liposomes as a catalase-powered nanomotor for effective cell uptake in cancer cells and plant leaves. *ACS Nano* **16**, 9019–9030 (2022).
41. Montis, C. et al. Shedding light on membrane-templated clustering of gold nanoparticles. *J. Colloid Interface Sci.* **573**, 204–214 (2020).
42. Wang, F. & Liu, J. Self-healable and reversible liposome leakage by citrate-capped gold nanoparticles: probing the initial adsorption/desorption induced lipid phase transition. *Nanoscale* **7**, 15599–15604 (2015).
43. Kariuki, R. et al. Behavior of citrate-capped ultrasmall gold nanoparticles on a supported lipid bilayer interface at atomic resolution. *ACS Nano* **16**, 17179–17196 (2022).
44. Cardellini, J. et al. Membrane phase drives the assembly of gold nanoparticles on biomimetic lipid bilayers. *J. Phys. Chem. C.* **126**, 4483–4494 (2022).
45. Cardellini, J. et al. Probing the coverage of nanoparticles by biomimetic membranes through nanoplasmonics. *J. Colloid Interface Sci.* **640**, 100–109 (2023).
46. Caselli, L. et al. A plasmon-based nanoruler to probe the mechanical properties of synthetic and biogenic nanosized lipid vesicles. *Nanoscale Horiz.* **6**, 543–550 (2021).
47. Riaz, M. et al. Surface functionalization and targeting strategies of liposomes in solid tumor therapy: a review. *Int. J. Mol. Sci.* **19**, 195 (2018).
48. Eloy, J. O., Petrilli, R., Trevizan, L. N. F. & Chorilli, M. Immunoliposomes: a review on functionalization strategies and targets for drug delivery. *Colloids Surf. B Biointerfaces* **159**, 454–467 (2017).
49. Bourganis, V. et al. On the synthesis of mucus permeating nanocarriers. *Eur. J. Pharm. Biopharm.* **97**, 239–249 (2015).
50. Cardellini, J. et al. Interaction of metallic nanoparticles with biomimetic lipid liquid crystalline cubic interfaces. *Front. Bioeng. Biotechnol.* **10**, https://doi.org/10.3389/fbioe.2022.848687 (2022).
51. Zendrini, A. et al. On the interaction and nanoplasmonics of gold nanoparticles and lipoproteins. *JCIS Open* **11**, 100088 (2023).
52. Wei, H. & Xu, H. Hot spots in different metal nanostructures for plasmon-enhanced Raman spectroscopy. *Nanoscale* **5**, 10794 (2013).
53. Salassi, S. et al. A martini coarse grained model of citrate-capped gold nanoparticles interacting with lipid bilayers. *J. Chem. Theory Comput.* **17**, 6597–6609 (2021).
54. Dallari, C. et al. Design and synthesis of novel Raman reporters for bioorthogonal SERS nanoprobes engineering. *Int. J. Mol. Sci.* **23**, https://doi.org/10.3390/ijms23105573 (2022).
55. Bozzuto, G. & Molinari, A. Liposomes as nanomedical devices. *Int. J. Nanomed.***10**, 975–999 (2015).
56. Brunetti-Pierri, N. & Scaglia, F. GM1 gangliosidosis: review of clinical, molecular, and therapeutic aspects. *Mol. Genet. Metab.* **94**, 391–396 (2008).
57. Tonin, R. et al. Pre-diagnosing and managing patients with GM1 gangliosidosis and related disorders by the evaluation of GM1 ganglioside content. *Sci. Rep.* **9**, 17684 (2019).
58. Capitini, C. et al. Fluorescent in situ staining and flow cytometric procedures as new pre-diagnostic tests for sialidosis, GM1 gangliosidosis and Niemann–pick type C. *Biomedicines* **10**, 1962 (2022).
59. Vasques, J. et al. Gangliosides in nervous system development, regeneration, and pathologies. *Neural Regen. Res.* **18**, 81 (2023).
60. Turkevich, J. Colloidal gold. part II - colour, coagulation, adhesion, alloying and catalytic properties. *Gold. Bull.* **18**, 125–131 (1985).
61. Turkevich, J., Stevenson, P. C. & Hillier. A study of the nucleation and growth processes in the synthesis of colloidal gold. *Discuss. Faraday Soc.* **11**, 55–75 (1951).
62. Montis, C., Maiolo, D., Alessandri, I., Bergese, P. & Berti, D. Interaction of nanoparticles with lipid membranes: a multiscale perspective. *Nanoscale* **6**, 6452–6457 (2014).
63. Zhao, J., Lui, H., Mclean, D. I. & Zeng, H. Automated autofluorescence background subtraction algorithm for biomedical Raman spectroscopy. *Appl. Spectrosc.* **61**, 1225–1232 (2007).

64. Feng, H. et al. Simple and rapid synthesis of ultrathin gold nanowires, their self-assembly and application in surface-enhanced Raman scattering. *Chem. Commun.* **15**, 1984–1986 (2009).
65. Jung, S. et al. Theragnostic PH-sensitive gold nanoparticles for the selective surface enhanced Raman scattering and photothermal cancer therapy. *Anal. Chem.* **85**, 7674–7681 (2013).
66. Chen, K. et al. A background-free SERS strategy for sensitive detection of hydrogen peroxide. *Molecules* **27**, https://doi.org/10.3390/molecules27227918 (2022).
67. Zhu, S. et al. Realization of high sensitive SERS substrates with one-pot fabrication of Ag–Fe3O4 nanocomposites. *J. Colloid Interface Sci.* **438**, 116–121 (2015).
68. Chen, L. et al. Surface-enhanced Raman scattering (SERS) active gold nanoparticles decorated on a porous polymer filter. *Appl. Spectrosc.* **71**, 1543–1550 (2017).

Acknowledgements

This work has been supported by the European Community through the BOW project (H2020-EIC-FETPROACT2019, ID 952183), by DoptoScreen project (Fondo di Beneficenza Intesa San Paolo 2019, B/2019/0289), RISE project, Regione Toscana (Bando Salute 2018) for the project Lysolate and PRIN 2022 (20228S5LWY). The authors acknowledge MIUR-Italy ("Progetto Dipartimenti di Eccellenza 2018–2022, ref B96C1700020008" allocated to the Department of Chemistry "Ugo Schiff"). Financial support was also provided by the "Integrated infrastructure initiative in photonic and quantum sciences—I-PHOQS" project financed by the EU next generation PNRR action and by PRIN 2022 PNRR: "Lipid Nanovectors for the Delivery of Nucleic Acids: a Composition-Structure-Function Relationship Approach (Lancelot)" - P2022RBF5P - CUP B53D23025810001 - "Finanziato dall'Unione europea – Next Generation EU" - Missione 4, Componente 2, Investimento 1.1 - Avviso MUR D.D. 1409 del 14/09/2022. We acknowledge the Florence Center for Electron Nanoscopy (FloCEN) at the University of Florence and the "Centro di competenza—RISE" funded by FAS Regione Toscana. The authors also wish to acknowledge Andrea Trabocchi, Riccardo Innocenti, and Elena Lenci (Department of Organic Chemistry, University of Florence) for their assistance in the experiments.

Author contributions

C. Dallari and J. Cardellini conceived the research and wrote the manuscript and contributed equally. D. Berti supervised the project. C. Dallari, J. Cardellini, L. Riccio, C. Ceni, I. De Santis, C. Credi, F.S. Pavone, C. Montis, M. Calamai, A. Morrone designed and performed all experiments and analyzed the data.

Competing interests

The authors declare no competing interests.

Additional information

Supplementary information The online version contains supplementary material available at https://doi.org/10.1038/s41467-024-52205-9.

Correspondence and requests for materials should be addressed to Debora Berti.

Peer review information *Nature Communications* thanks Dorleta Jimenez de Aberasturi, and the other, anonymous, reviewer(s) for their contribution to the peer review of this work. A peer review file is available.